Progress In Electromagnetics Research C, Vol. 83, 83–96, 2018

An Efficient Algorithm for the Analysis and Design of Carbon Nanotube Photonic Crystals

Said Mikki[1, *] and Ahmed Kishk[2]

Abstract—We develop an efficient algorithm for the computation of the complete transmitted and reflected electromagnetic fields in generic 2D arrays of carbon nanotubes (CNTs). The method relies on first approaching individual CNTs using an effective-boundary condition based on a proper quantum conductivity model. An exact eigenmode solution is obtained for this problem for both single-wall and multi-wall CNTs, which then is integrated with Floquet mode theory to handle periodic arrays of CNTs. The algorithm's convergence rate is accelerated using special methods and then applied to the analysis and design of various multi-layered CNT-based photonic crystal devices. It is shown that the proposed method can clearly demarcate the intrinsic optical resonances due to electronic transitions in individual CNTS and new sets of "geometric" optical resonances produced by the array spatial structure. The algorithm can be used to analyze measured optical spectra of CNT composites and to design new nanomaterial-engineered optical bandgap devices.

1. INTRODUCTION

Carbon nanotubes (CNTs), first reported in [1], are crystal structures in the form of single (or multiple cocentric) cylindrical tubes with high aspect ratio. They have been proposed as candidates for various applications, ranging from enhancement of the mechanical properties of composites to logical gates in new genre of nano-electronic devices [2–4]. The fact that they can function as either metallic or semiconducting, depending on the geometric structures, has attracted the attention of many researchers, leading to systematic investigations of their performance under wide range of conditions. In recent years, one particular application has attracted attention in CNT research, and that is the possibility of assembling photonic crystal devices using CNTs as fundamental building units. Experimental ideas were explored in [5], while multi-walled carbon nanotubes were analyzed in [6]. More recently, the possibility of setting up negative refraction in CNT-based photonic crystals was investigated [7]. Photonic crystals, being periodic arrangements of identical units, can act like optical filters since they tend to permit wave transmission only within certain bands. Since CNTs exhibit a plethora of unusual electrical and mechanical properties at the nanoscale, it is important to explore the ability to design new optical devices based on manipulations of the geometric arrangements of CNT unit cells embedded into a larger periodic structure. Indeed, the main task of the present paper is to propose such possible computational method. While many investigations of arrays of CNTs has been reported, they tend to rely either on full-wave numerical solution or measurement. Both could be tedious in early R&D stages that require repeated use of the same calculation with different parameter values, for example as in optimization. There is a need to develop an efficient method intermediate in complexity between exact solutions and fully-numerical ones. This paper will propose such an algorithm based on combining the effective-boundary condition method and Floquet mode theory.

Received 10 February 2018, Accepted 20 March 2018, Scheduled 10 April 2018
* Corresponding author: Said Mikki (smikki@newhaven.edu).
[1] Department of ECECS, University of New Haven, West Haven, Connecticut, United States. [2] University of Concordia, Montreal, Canada.

Since CNTs have characteristic scale (diameter) in the nanometer range, the electromagnetic spectrum pertinent to their fundamental (electronic resonances) tend to be in the optical range, though microwave properties of CNT-based composites have been investigated. While numerous experimental measurements of the optical spectra of CNTs have been reported over the year, it remains challenging to compute the scattered field from first principles, first because of the lack of exact knowledge of the geometry and structure at the nanoscale, and second since electromagnetic theory, usually successful at the computational level in the macroscopic scale, cannot be directly applied at the microscopic scale. Here, we provide a theoretical description of the electromagnetic scattering by both single- and multi -wall carbon nanotubes based on an effective-boundary condition derived previously using a phenomenological quantum model [8–10]. The analytical solution for the scattering problem developed by the authors for single-wall CNT in [11, 12] was compared with experiments and good results had been obtained. The method was than then generalized to include multi-wall CNT [13–15]. In this paper, we undertake the task of extending the electromagnetic scattering model developed in [11] and [15] to multi-layered arrays of single- and multi- walled CNTs.

There are several practical motivations for undertaking such a study. First, actual CNT composites hardly contain isolated tubes. Instead, each composite contains a large number of nanotubes arranged in various ways. Spectroscopic data obtained by scattering experiments constitute the main empirical input for theoretical models constructed to understand the fundamental physics of those nanostrucutres. Having a theoretical model for the electromagnetic response helps in understanding measurement data. Second, CNTs can be used in the design of new nanophotonic devices by aligning them in various configurations. A theoretical model is indispensable for the prediction and development of practical devices since it will provide *a priori* insight into the new physics associated with using CNTs instead of other, more conventional, materials. Also, a simulation code can cut the R&D cost by producing primitive prototypes before going to the fabrication process.

Figure 1 illustrates the general geometry of the problem dealt with in this paper. Each circle denotes a fictitious unit cell in which arbitrary periodic arrangements of CNTs can be assumed. The generalized reflection matrix of the unit cell can be found using the recursive T-matrix algorithm [18]. The problem then shifts to the determination of the fields everywhere using the periodic Green functions, or, equivalently, the lattice sum formalism. We adopt here the latter approach and combine it with the exact electromagnetic effective-boundary condition solution developed earlier in order to determine the field everywhere. A special acceleration method is applied to speed up the computation of the lattice sum. The theory of Floquet modes is deployed in order to complete the determination of the fields and hence the transmission and reflection characteristics of generic CNT-based photonic crystals. Numerical examples are included. The intrinsic resonances (electronic transitions) are clearly distinguishes from the geometric resonances due to the array factor effect of the photonic crystal. It is shown by a design

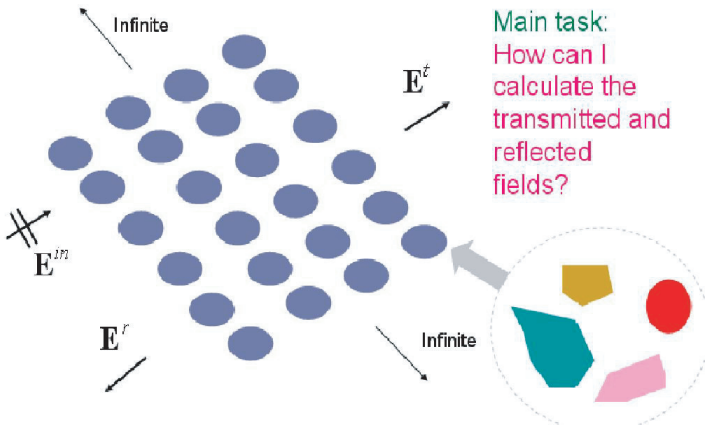

Figure 1. General setting for the 2D semi-finite photonic crystal. The main problem is to calculate the reflected and transmitted field, due to an incident field, given the generalized reflection matrix of the circular unit cell.

example that optimizing the geometric parameters of the CNT array can lead to desired transmission characteristics.

Dealing with *random* arrays of CNT can still be made using our algorithm. Since the method is very efficient, it is possible to perform statistical analysis by allowing the position of each CNT to become a random variable and then computing the expected values of the transmission and reflected coefficients of the total random array using large number of computational runs. This is in fact one of the main advantages of the method proposed in this paper. Indeed, full-wave commercial solvers cannot deal with the complete electromagnetic numerical solution in efficient manner. Since we solve the electromagnetic boundary-value problem analytically and then accelerate the convergence of the results, the results obtained by our method are expected to play a significant role in analysis conducted with measurements of random CNT arrays where the positions and numbers of CNTs are unknown. For examples on how to combine electromagnetic analysis with statistical consideration, see [16, 17].

2. THE ELECTROMAGNETIC MODEL OF ISOLATED CARBON NANOTUBES

2.1. Review of the Structure of Carbon Nanotubes

Figure 2 illustrates the honeycomb lattice structure of graphene†. The unit cell is specified by two atoms located at the positions $1/3(\mathbf{a}_1 + \mathbf{a}_2)$ and $2/3(\mathbf{a}_1 + \mathbf{a}_2)$, where $\mathbf{a}_1$ and $\mathbf{a}_2$ are two unit vectors defining the lattice constants and $b_0 = |\mathbf{a}_1| = |\mathbf{a}_2| = 0.142\,\text{nm}$ is the interatomic distance. The CNT is formed by rolling up this sheet such that the circumference of the tube coincides with the chiral vector $\mathbf{c} = m\mathbf{a}_1 + n\mathbf{a}_2$. Here m and n are two integers that completely determine the structure and the properties of the CNT. If only one layer is used to form the tube, the resulting structure is called single-wall CNT (SWCNT). Alternatively, if the tube consists of several co-centric cylinders, we call it multi-wall CNT (MWCNT). CNTs with the structure $(n, 0)$ are called *zig-zag* CNT because the pattern created along the circumference of the tube resembles a zig-zag motion. The structure (n, n) is called *armchair*. Tubes that have $0 < n \neq m$ are called *chiral*. The radius of the CNT is given by [4]

$$b = \frac{|\mathbf{c}|}{2\pi} = \frac{b_0}{2\pi}\sqrt{m^2 + mn + n^2}. \tag{1}$$

One of the most important features of CNTs is their ability to work in different transport modes depending on the geometry, which is completely specified by the integers m and n. Armchair CNTs are always metallic since the resulting energy diagram has no energy bandgap. Zig-zag tubes can be

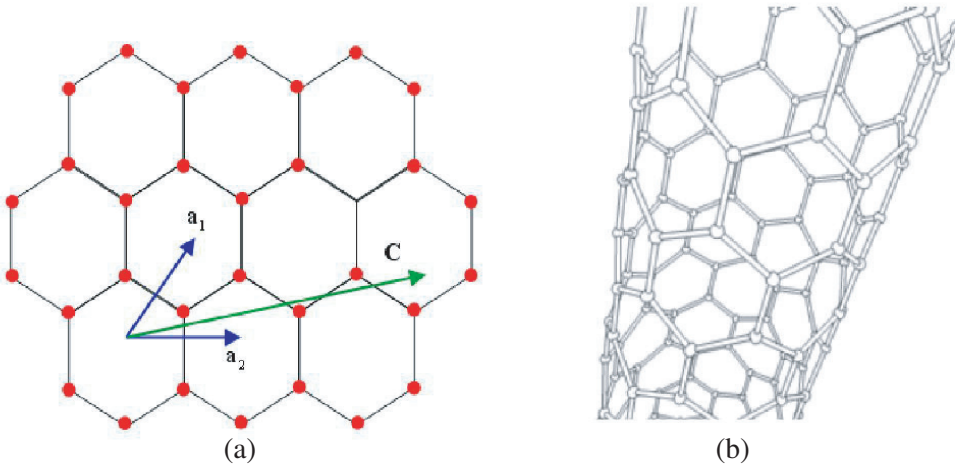

Figure 2. (a) Graphene sheet used in forming CNTs (The dots illustrate the carbon atoms positions.) (b) Geometry of a single-wall carbon nanotube (SWCNT).

† Graphene is defined as a 2D layer of graphite.

either metallic or semiconducting depending on the chirality (i.e., the ratio m/n). If $m = 3i$, where i is an integer, then the resulting CNT will be metallic. Otherwise, a non-zero bandgap will exist and the properties of the structure becomes closer to semiconductors.

2.2. The Effective-Boundary Condition Approach to the Electrodynamics of Single-Wall Carbon Nanotubes (SWCNTs)

In CNTs, the so called π-electron, which belongs to an unsaturated orbital orthogonal to the tube surface, is relatively free and can therefore respond to an external electromagnetic fields [4]. The interaction of this electron with external electromagnetic field leads to postulating an effective conductivity function describing the current induced by the interaction. The idea of the effective-boundary condition is to replace a microscopic fine crystal structure of matter, in this case the carbon nanotube atomic lattice arranged in a cylindrical fashion, by an effective, homogenized surface in which the behavior of the electromagnetic field on the two sides of the surface can be described by formulas familiar to conventional macroscopic electromagnetism. The effective-boundary condition is given by [9]

$$\hat{n} \times \left(\mathbf{E}^1 - \mathbf{E}^2\right) = 0,\ \hat{n} \times \left(\mathbf{H}_z^1 - \mathbf{H}_z^2\right) = 0 \tag{2}$$

$$\left\{1 + \Upsilon\left(\omega\right) \partial^2 / \partial z^2\right\} \hat{n} \times \left(\mathbf{H}_\varphi^2 - \mathbf{H}_\varphi^1\right) = \sigma_{\mathrm{cn}}\left(\omega\right) \left(\hat{z} \cdot \mathbf{E}\right) \hat{z}, \tag{3}$$

where the unit normal vector $\hat{n}$ is directed outward to the surface of the CNT. Here, $\Upsilon(\omega)$ represents the effect of spatial dispersion in the z-direction and is given by $\Upsilon(\omega) = l_0/[(\omega/c)(1 - j/\omega\tau)]$, where, l_0 is estimated to be around 10^{-5} for metallic tubes [9]. The azimuthal current of the CNT is very weak compared to the axial component and therefore is ignored in the boundary conditions above. The axial conductivity for armchair CNT is given by [8, 9]

$$\sigma_{\mathrm{cn}}\left(\omega\right) = \frac{je^2\omega}{\pi^2\hbar\rho_{\mathrm{cn}}} \left\{ \frac{1}{\omega\left(\omega - j\nu\right)} \sum_{s=1}^{m} \int dp_z \frac{\partial F_c}{\partial p_z} \frac{\partial \mathcal{E}_c}{\partial p_z} + 2 \sum_{s=1}^{m} \int dp_z \mathcal{E}_c \left|R_{vc}\right|^2 \frac{F_c - F_v}{\hbar^2\omega\left(\omega - j\nu\right) - 4\mathcal{E}_c^2} \right\}, \tag{4}$$

where ν is the *relaxation frequency*, which is related to the *relaxation time* τ by $\nu = \tau^{-1}$. The normalized Planck's constant is given by $\hbar \approx 1.05457 \times 10^{-34}\mathrm{J} \cdot \mathrm{s}$ and the electron charge $e \approx 1.6022 \times 10^{-19}\,\mathrm{C}$. On the other hand, the well-known dispersion relation of CNTs is given by

$$\mathcal{E}_{c,v}\left(p_z, s\right) = \pm\,\gamma_0 \sqrt{1 + 4\cos\left(\frac{\pi s}{m}\right)\cos\left(\frac{d}{\sqrt{3}}p_z\right) + 4\cos^2\left(\frac{d}{\sqrt{3}}p_z\right)}, \tag{5}$$

where p_z is the quasi-momentum in the z-direction, $d = 3a_0/2\hbar$, and the positive and negative signs in Eq. (5) corresponds to the conduction and valence bands, respectively. The classical equilibrium Fermi distribution can be calculated by

$$F_{c,v} = \frac{1}{1 + \exp\left(\mathcal{E}_c / k_B T\right)}, \tag{6}$$

where $k_B = 1.381 \times 10^{-23}\,\mathrm{J/K}$ is Boltzmann's constant, and T is the absolute temperature. Finally, the matrix element for armchair CNT is determined by means of

$$R_{vc}\left(p_z, s\right) = \frac{\sqrt{3}a_0\gamma_0^2}{2\mathcal{E}_c^2} \sin\left(\frac{d}{\sqrt{3}}p_z\right) \sin\left(\frac{\pi s}{m}\right). \tag{7}$$

The integrals in Eq. (4) are calculated in the first Brillouin zone. One possible zone is the integrations limits $p_z = \pm 2\pi\hbar/\sqrt{3}a_0$. The numerical cost for calculating the quantum conductivity in Eq. (4) increases dramatically with large m.

2.3. The Effective-Boundary Condition Approach to the Electrodynamics of Single-wall and Multi-Walled Carbon Nanotubes

Based on the quantum conductivity derived in Section 2.2, the authors used exact eigenfunction expansions in electromagnetics to solve the problem of electromagnetic scattering by CNTs and obtained numerical results in good agreement with experiments [11]. Since eigenfunction expansions in more

general form will be developed below (see Section 3.1) using Floquet theory, we will not review the older results here. However, we mention that the method developed in [11] for SWCNT has been extended to treat MWCNTs in [13, 14], again using the effective-boundary condition method. The basic idea was to solve analytically for multiple reflections inside every cylindrical regions using standard recursive algorithms in electromagnetics. The resulting algorithm in [13, 14] can be used to compute electric and magnetic fields in all regions of the multi-walled CNT structure, with an arbitrary number of wall and chirality for each layer.

3. THE FLOQUET MODE THEORY OF ELECTROMAGNETIC SCATTERING BY CNT ARRAYS

3.1. The 1-D Infinite Array Case

We start first by solving the problem of single layer, or an infinite array of cylindrical unit cells as shown in Fig. 3. The incident field can be expanded in cylindrical modes as follows [18, 21]

$$E^{in} = \left[J_n\left(k_\rho \rho_0\right) e^{-jn\varphi}\right]^T \cdot \mathbf{a}^{in}, \tag{8}$$

where

$$\left[J_n\left(k_\rho \rho_0\right) e^{-jn\varphi}\right]^T = \left[\begin{array}{ccccccccc} J_{-N}\left(k_\rho \rho_0\right) e^{-jn\varphi} & \ldots & \ldots & 0 & \ldots & \ldots & J_N\left(k_\rho \rho_0\right) e^{-jn\varphi} \end{array}\right]^T \tag{9}$$

and $\mathbf{a}^{in} = [j^n e^{jn\phi} e^{jk_z z}]$. Here, $J_n(x)$ is the bessel function of the first kind. The scattered field is written as

$$E^{sc} = \sum_{l=-\infty}^{\infty} \left[H_n^{(2)}\left(k_\rho \rho_l\right) e^{-jn\phi_l}\right]^T \cdot \mathbf{a}_0^{sc} e^{jk_\rho lh\cos\phi^{in}}, \tag{10}$$

where $\mathbf{a}_0^{sc}$ is the scattering amplitude of the 0th unit cell. Now consider the fields within the 0th unit cell, i.e., we restrict our observations only to space points where $\rho_0 = \sqrt{x^2 + y^2} < h$. In this case, using the addition theorem, we arrive at

$$\left[H_n^{(2)}\left(k_\rho \rho_l\right) e^{-jn\phi_l}\right] = \left[H_n^{(2)}\left(k_\rho \rho_0\right) e^{-jn\phi_l}\right]^T \cdot \left[H_{n-m}^{(2)}\left(k_\rho lh\right)\right]. \tag{11}$$

Therefore, the total field $E^{\text{total}} = E^{\text{in}} + E^{\text{sc}}$ can be decomposed as

$$E^{\text{total}} = \left[J_n\left(k_\rho \rho_0\right) e^{-jn\varphi}\right]^T \cdot \left\{\mathbf{a}^{in} + \bar{\bar{L}} \cdot \mathbf{a}_0^{sc}\right\} + \left[H_n^{(2)}\left(k_\rho \rho_0\right) e^{-jn\phi_l}\right]^T \cdot \mathbf{a}_0^{sc}. \tag{12}$$

where the lattice sum is given by [19]

$$L_{mn} = S_{m-n}\left(k_\rho h, \phi^{in}\right) = \sum_{\substack{l=-\infty \\ l\neq 0}}^{\infty} H_n^{(2)}\left(k_\rho lh\right) e^{jk_\rho lh\cos\phi^{in}}. \tag{13}$$

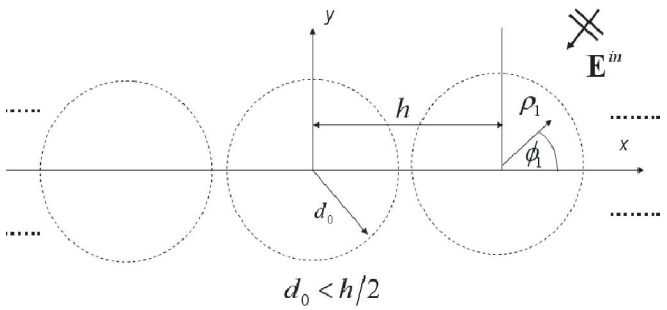

Figure 3. A diagram of the geometry of the general 1-D scattering problem by infinite array of cylindrical unit cells.

Finally, the recursive T-matrix algorithm immediately allows us to write [18]

$$\mathbf{a}_0^{sc} = \left[1 - \bar{\bar{L}} \cdot \bar{\bar{R}}\right]^{-1} \bar{\bar{R}} \cdot \mathbf{a}^{in}. \tag{14}$$

The convergence of the lattice sum in Eq. (13) is extremely slow, leading to high computational demand when being employed in numerical calculations of the fields scattered by multi-layered arrays. Fig. 4 illustrates the calculation of S_0 at a single point of its argument plotted versus the number of terms required in the direct calculation of the sum. Clearly such incredibly large number of terms is unacceptable since the bottle neck of the array problem is the computation of the lattice sum. Fortunately, an alternative acceleration technique is available in literature in which the lattice sum was converted to a numerical integration [20]. We implemented a subroutine to calculate the lattice sum and compared the results with direct method. Fig. 5 illustrates the computed sum versus the number of integration points required. Here, a refers to the truncation upper limit of the (theoretically infinite) integral. A simple trapezoidal rule was utilized in the code. It is found that a number of integration points as low as 1000 is enough to obtain accurate results for practical cases of interest.

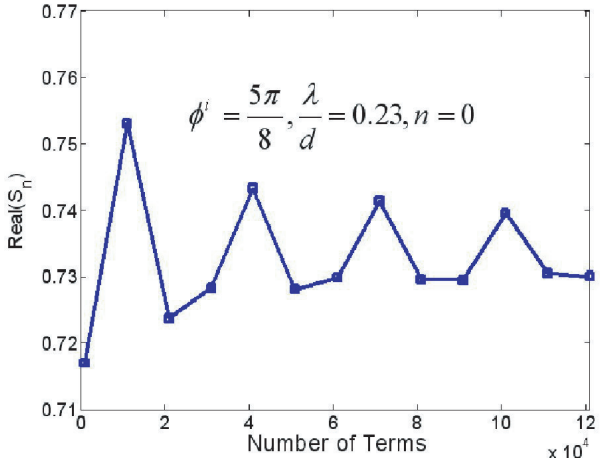

Figure 4. Direct calculation of the lattice sum in Eq. (13).

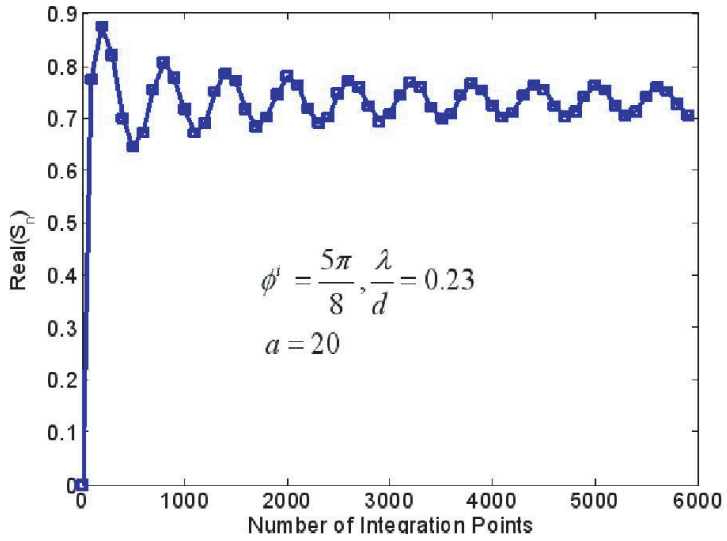

Figure 5. Indirect calculation of the lattice sum in Eq. (13) using an the acceleration procedure in [20].

The last step needed to complete the electromagnetic solution of the problem is to transform the cylindrical coordinates solution into plane wave (Floquet) series expansion. Utilizing the well-known Hankel function transformation [18], the needed scattered and transmitted fields can be written as

$$E^{sc} = \sum_{l=-\infty}^{\infty} \mathbf{p}_l^T \cdot \mathbf{a}_0^{sc} e^{-j\left(k_{xl}x+k_{yl}y\right)}, E^t = \sum_{l=-\infty}^{\infty} \left(\delta_{l0} + \mathbf{q}_l^T \cdot \mathbf{a}_0^{sc}\right) e^{-j\left(k_{xl}x+k_{yl}y\right)}, \tag{15}$$

respectively. Here, we have

$$k_{xl} = -k_\rho \cos\phi^{in} + 2l\pi/h, k_{yl} = \sqrt{k_0^2 - k_{xl}^2}, \tag{16}$$

where [19]

$$p_v = \begin{bmatrix} \dfrac{2j^m \left(k_{xl} - jk_l\right)^m}{hk_v k_0^m} & m \geq 0 \\ \dfrac{2j^{|m|} \left(k_{xl} + jk_l\right)^{|m|}}{hk_v k_0^{|m|}} & m < 0 \end{bmatrix}, q_v = \begin{bmatrix} \dfrac{2j^m \left(k_{xl} + jk_l\right)^m}{hk_v k_0^m} & m \geq 0 \\ \dfrac{2j^{|m|} \left(k_{xl} - jk_l\right)^{|m|}}{hk_v k_0^{|m|}} & m < 0 \end{bmatrix}. \tag{17}$$

Note that now power reflection and transmission coefficients can be immediately obtained by

$$R_l = \frac{k_k}{k_\rho \sin\phi^{in}} \left|\mathbf{p}_l^T \cdot \mathbf{a}_0^{sc}\right|^2, T_l = \frac{k_k}{k_\rho \sin\phi^{in}} \left|\delta_{l0} + q_l^T \cdot \mathbf{a}_0^{sc}\right|^2, \tag{18}$$

respectively. Fig. 6 provides a verification of our code by direct comparison with data in [19]. In this result, we used a total number of ± 14 cylindrical modes and ± 7 space modes.

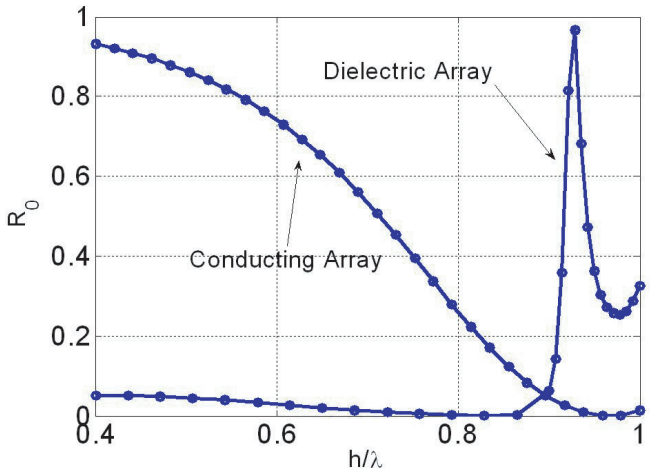

Figure 6. Comparison of our code with [19]. Here, for the data for the dielectric cylinder are $\varepsilon_r = 2.0$, $d = 0.3\lambda$ and for the conducting case $|\varepsilon_r| = \infty$, $d = 0.15\lambda$. The dotted data are those in [19].

3.2. Multi-Layer Array Structures

The passage to the multi-layer array case can be accomplished easily by applying the generalized scattering matrix method. Fig. 7 illustrates the general geometry of the problem. Wetreat each layer as a "system" with a reflection and transmission matrices that are determined by Eqs. (15)–(18). The (generalized) reflection and transmission matrices of the total structure are found by computing the cascaded connection matrix of the various sub-blocks recursively in a way similar to the algorithm of Section 3.1. The most important condition for the applicability of the generalized scattering matrix method is the ability to draw a fictitious line (the dashed curved line in Fig. 7) between every two

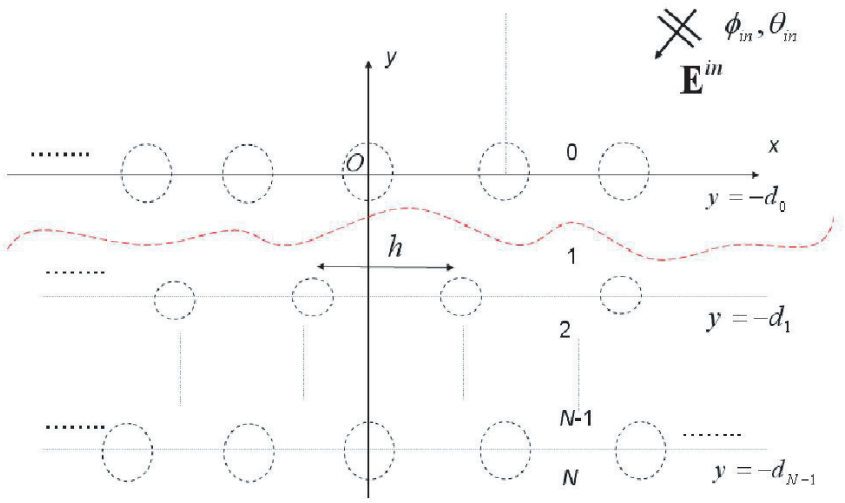

Figure 7. Geometry of the multi-layer problem.

layers without crossing through any circular unit cell. In this case, the fields in the space between the layers can be expanded as linear combinations of growing and decaying exponentials, in addition to propagating waves, while the fields in the outermost and innermost layers can admit only propagating or/and evanescent modes.

3.3. The CNT Array Floquet Mode Algorithm

The basic content of the Floquet mode algorithm is shown in Fig. 8. The algorithm input is an excitation plane wave, while the output is a series of space harmonics (or Floquet modes) describing the field everywhere. Due to the symmetry of the problem, it would be much easier to convert incident plane waves to cylindrical harmonics using the space-to-cylindrical transformation of Section 3.1. The

Input *single* Space Mode $\mathbf{E}=\mathbf{E}_0 e^{-j\mathbf{k}_0\cdot\mathbf{r}}$

Intermediate cylindrical mode $\mathbf{E}=\mathbf{E}_0\sum_{n=-\infty}^{\infty} j^n J_n\left(k_\rho\rho\right)e^{jn\left(\phi-\phi_0\right)}e^{-jk_z z}$

Infinite number of Space Modes

$$k_{xl}=-k_\rho\cos\phi^{in}+2l\pi/h,\ k_{yl}=\sqrt{k_0^2-k_{xl}^2}$$

$$E^t=\sum_{l=-\infty}^{\infty}\left(\delta_{l0}+\mathbf{q}_l^T\cdot\mathbf{a}_0^{sc}\right)e^{-j\left(k_{xl}x+k_{yl}y\right)}\quad E^{sc}=\sum_{l=-\infty}^{\infty}\mathbf{p}_l^T\cdot\mathbf{a}_0^{sc}e^{-j\left(k_{xl}x+k_{yl}y\right)}$$

Figure 8. The various transformation (thick downward arrows) employed in the generalized scattering matrix method applied to the problem of arbitrary multi-layered structures.

kernel scattering problem is then solved, and the solution is converted back to space harmonics. Since the details of the transformations are both straightforward and quite lengthy, we just report the final results in the appendices at the end of this paper.

Before moving to numerical results, we mention that in most practical settings, CNT arrays come with structural defects rendering the exact periodic boundary condition implied by the use of Floquet mode theory an approximation, not an exact one. Indeed, it is well known that composites of CNT unit cells often exhibit structural differences making not all unit cells identical [22]. Those defects have been characterized by various experimental methods, for instance X-ray [23]. In general, new physics could emerge if the disorder introduced by defects can lead to the excitation of new modes or the localization of energy around the defect [24]. Complete theoretical analysis of these new physical phenomenon induced by strong mode coupling caused by CNT defects are beyond the scope of the present paper. However, the general and computationally efficient Floquet mode theory developed here can provide a solid basis for constructing an extension of the present method taking into account changes in the nanostrucutres of the CNT photonic crystals due to local violations of periodicity.

4. NUMERICAL EXAMPLES

4.1. Basic Analysis Case

For the following numerical examples, we calculate the fundamental mode power reflection coefficient R_0 as given by Eq. (18), with ± 3 space modes and ± 3 cylindrical modes. Notice that in the general formalism adopted here, the power coefficient R_0 *does* take into account the interaction of higher-order (propagating and evanescent) modes between the layers (in this case up to three spatial modes). In other words, due to spatial dispersion (non-locality), even the main (fundamental) mode is function of the higher-order modes connecting the interactions between the various layers of the structures.

In Fig. 9, we show the computed scattered field for 8-layer arrays of $(10, 10)$ SWCNTs. The y-direction spacing d is denoted by d_y and we choose to relate it to the x-direction spacing h, denoted here by d_x, by $d_y = 0.75d_x$. We also assume $\varphi_{in} = 90^\circ$ and $\theta_{in} = 90^\circ$. The figure also shows the quantum conductivity of an isolated SWCNT for comparison. It is evident from the data that the observed spectral response of the array structure introduces new resonances different from the fundamental resonances of the individual nanotube. Strictly speaking, certain resonances in the spectrum of the array environment results from multiple reflections of the (propagating and/or evanescent) waves between internal layers, giving rise to new resonance peaks in the observed output. As spectroscopic data,

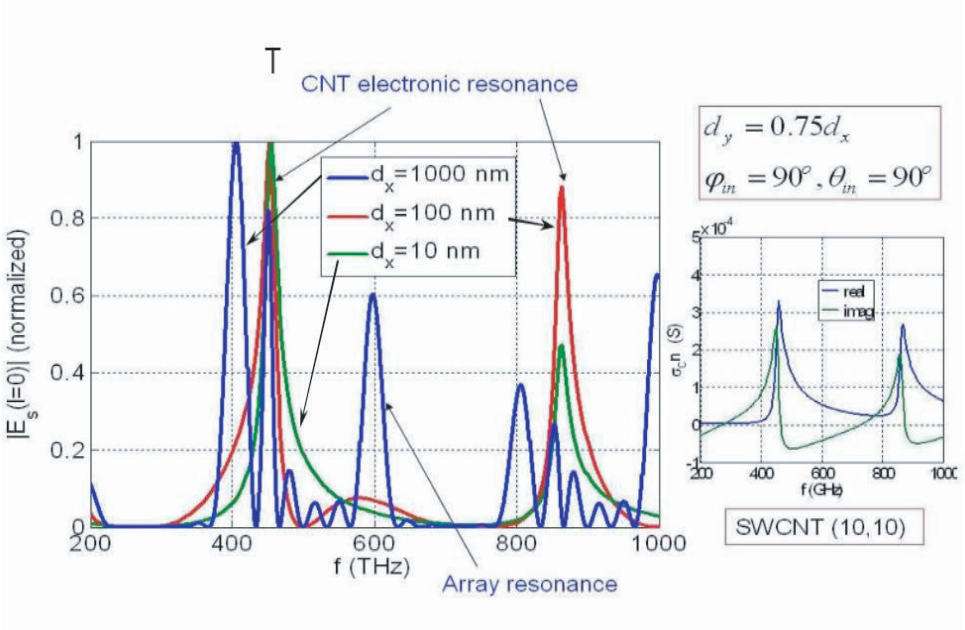

Figure 9. Computed scattered field by 8-layer array of SWCNTs.

those should be distinguished from the CNT resonances that are due to intra- and inter-band electronic transition.

4.2. CNT Nano-Photonic Crystal Design Case Study

In the next example, we provide simple examples illustrating the design of photonic bandgap structure implemented using SWCNTs and MWCNTs. Fig. 10 illustrates the spectral responses for 1-layer, 12-layer, and 30-layer photonic crystals. As expected, when the number of layers increases, the structure approaches a limit state of quasi-2-D periodicity (the y-direction periodicity is approximate, but the x-direction one is exact), where the familiar stopband periodic repetition is reproduced. Therefore, when the remaining parameters of the structure are chosen properly (in this case through manual tuning but the process can be easily automated through optimization methods), it is possible to achieve complete stopband (passband) at desired frequency range when the total waves scattered by the individual unit cells interact destructively (constructively). The figure also shows the conductivity of the isolated SWCNT. It is evident that the normalized response of 1-layer array is indistinguishable from the isolated array, due to the weakness of the coupling in the x-direction in this particular example. As more CNT 1D layers are inserted, geometric interactions (array effects) dominate, and the response is drastically changed to produce bandgap structures.

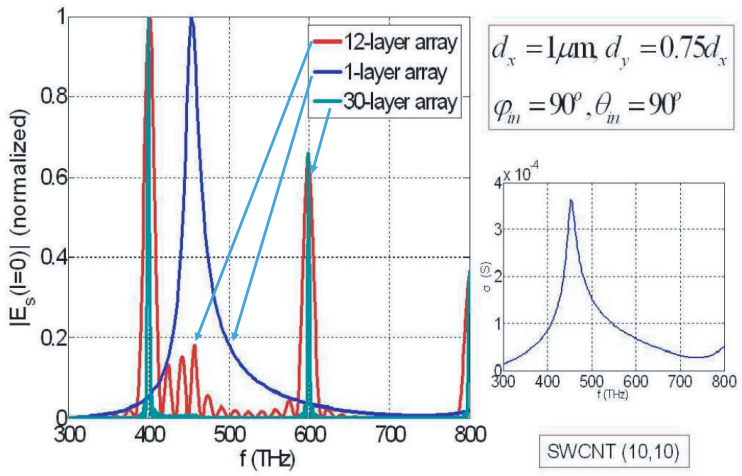

Figure 10. Design of bandgap structure using SWCNTs.

Figure 11 illustrates the scattering spectrum of 2-layer array of MWCNTs. We assume that all of the nanotubes are identical and composed of only 4 walls with the armchair structure $(10, 10)$, $(20, 20)$, $(30, 30)$, $(40, 40)$. (This particular geometry fits with the observed radius of MWCNTs obtained by electron scanning experiments.) The dimensions of the array are $d_y = 0.75 d_x$ and we assume normal incidence. It is observed again that changing the dimensions of the array introduces new resonances.

Finally, in Fig. 12 we provide the angle response of a 6-layer photonic crystal. It is evident that the while the structure may be optimized to work at certain angle of incidence, the response introduces new behavior at other angles. In this particular example, a redshift in the resonance structure of the spectral response was observed with increasing angle of incidence.

We note that the number of layers in photonic crystals controls the complexity of the performance of the system acting as a spatio-temporal filter. For instance, adding more layers will result in additional geometrical resonances due to the creation of more multiple-reflection pathways between the various layers in the overall array. The situation can be compared with designing multiple-stages or cascaded filters in circuit theory, where adding more stages increases the number of resonances and hence tend to increase the passband bandwidth or improve stopband attenuation performance (or both). Simulation results performed using our algorithm have demonstrated similar effects where the stopband and passband bandwidthes could be controlled indeed by adding more layers.

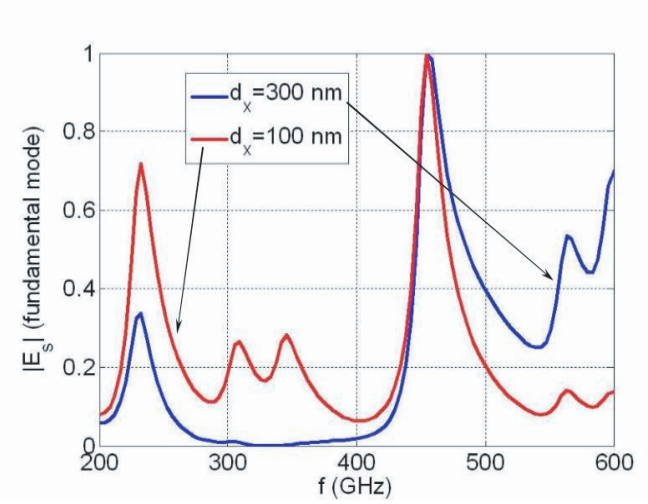

Figure 11. Scattering spectrum for 2-layer array of identical MWCNTs. Each MWCNT is composed of $(10, 10)$, $(20, 20)$, $(30, 30)$, $(40, 40)$ co-centric tubes. Here $d_y = 0.75d_x$, $\varphi_{in} = 90°$, $\theta_{in} = 90°$.

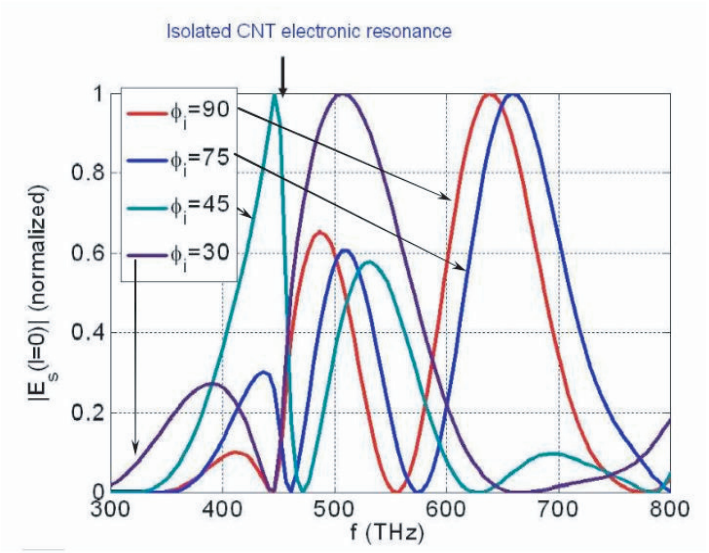

Figure 12. The angle response of 6-layer array of SWCNTs. Here $d_x = 100\,\text{nm}$, $d_y = 0.75d_x$, $\varphi_{in} = 90°$, $\theta_{in} = 90°$.

5. CONCLUSION

We combined exact eigenmode solution of isolated carbon nanotubes, obtained via an effective-boundary condition approach, with Floquet mode theory in order to construct and algoithm capable of predicting the transmission properties of generic 2D CNT-based crystals. The algorithm appears to distinguish between intrinsic and geometric resonances and is shown to be efficient by using a special method to accelerate the convergence of the lattice sum. Several examples were introduced, including design of stopband optical device by controlling spacing and CNT types. The algorithm, being computationally efficient, can be deployed in optimization of more complex nanoscale photonic crystals. It is found that the algorithm can be used to distinguish electronic transition resonances in CNTs from new geometric resonances produced by the array structure of the photonic crystals.

APPENDIX A. DOWN-GOING CANONICAL CASE

Let N and M be the total numbers of cylindrical and space modes, respectively. For the down-going case, we solve the problem of scattering by a series of plane waves incident on the structure (as shown in Fig. 7) with $\mathbf{k}_z \cdot \hat{z} < 0$. In this case, the reflection and transmission matrices for a single layer are read off the results of Section 3.1 as

$$\underbrace{\bar{\mathbf{R}}_{i,i+1}}_{M\times M} = \underbrace{\bar{\mathbf{U}}}_{M\times N} \cdot \left(1 - \underbrace{\bar{\mathbf{R}}_i}_{N\times N} \cdot \underbrace{\bar{\mathbf{L}}}_{N\times N}\right)^{-1} \cdot \underbrace{\bar{\mathbf{R}}_i}_{N\times N} \cdot \underbrace{\bar{\mathbf{P}}^{\text{in}}}_{N\times M} \tag{A1}$$

and

$$\underbrace{\bar{\mathbf{T}}_{i,i+1}}_{M\times M} = \bar{\mathbf{I}} + \underbrace{\bar{\mathbf{V}}}_{M\times N} \cdot \left(1 - \underbrace{\bar{\mathbf{R}}_i}_{N\times N} \cdot \underbrace{\bar{\mathbf{L}}}_{N\times N}\right)^{-1} \cdot \underbrace{\bar{\mathbf{R}}_i}_{N\times N} \cdot \underbrace{\bar{\mathbf{P}}^{\text{in}}}_{N\times M}, \tag{A2}$$

where

$$\bar{\mathbf{U}} = [u_{mn}] = \left[\frac{2j^n}{k_0 h \sin\phi_m} e^{-jn\phi_m}\right], \ \bar{\mathbf{V}} = [v_{mn}] = \left[\frac{2j^n}{k_0 h \sin\phi_m} e^{jn\phi_m}\right], \tag{A3}$$

$$\bar{\mathbf{P}}^{\text{in}} = \left[j^n e^{jn\phi_m}\right], \bar{\mathbf{R}}_i = \bar{\beta}_{0,i} \cdot \bar{\tilde{\mathbf{R}}}_i \cdot \bar{\beta}_{i,0}, \tag{A4}$$

for which we have $n = 0, \pm 1, \pm 2, \ldots, N$ and $m = 0, \pm 1, \pm 2, \ldots, M$.

APPENDIX B. UP-GOING WAVE CANONICAL CASE

For the up-going case, we solve the problem of scattering by a series of plane waves incident on the structure (as shown in Fig. 7) with $\mathbf{k}_z \cdot \hat{z} > 0$. In this case, the reflection and transmission matrices for a single layer are read off the results of Section 3.1 as

$$\underbrace{\bar{\mathbf{R}}_{i+1,i}}_{M\times M} = \underbrace{\bar{\mathbf{V}}}_{M\times N} \cdot \left(1 - \underbrace{\bar{\mathbf{R}}_i}_{N\times N} \cdot \underbrace{\bar{\mathbf{L}}}_{N\times N}\right)^{-1} \cdot \underbrace{\bar{\mathbf{R}}_i}_{N\times N} \cdot \underbrace{\bar{\mathbf{Q}}^{\text{in}}}_{N\times M} \tag{B1}$$

and

$$\underbrace{\bar{\mathbf{T}}_{i+1,i}}_{M\times M} = \bar{\mathbf{I}} + \underbrace{\bar{\mathbf{U}}}_{M\times N} \cdot \left(1 - \underbrace{\bar{\mathbf{R}}_i}_{N\times N} \cdot \underbrace{\bar{\mathbf{L}}}_{N\times N}\right)^{-1} \cdot \underbrace{\bar{\mathbf{R}}_i}_{N\times N} \cdot \underbrace{\bar{\mathbf{Q}}^{\text{in}}}_{N\times M}, \tag{B2}$$

where

$$\bar{\mathbf{U}} = [u_{mn}] = \left[\frac{2j^n}{k_0 h \sin\phi_m} e^{-jn\phi_m}\right], \ \bar{\mathbf{V}} = [v_{mn}] = \left[\frac{2j^n}{k_0 h \sin\phi_m} e^{jn\phi_m}\right], \tag{B3}$$

$$\bar{\mathbf{R}}_i = \bar{\beta}_{0,i} \cdot \bar{\tilde{\mathbf{R}}}_i \cdot \bar{\beta}_{i,0}, \bar{\mathbf{Q}}^{\text{in}} = \left[j^n e^{-jn\phi_m}\right], \tag{B4}$$

for which we have $n = 0, \pm 1, \pm 2, \ldots, N$ and $m = 0, \pm 1, \pm 2, \ldots, M$. Here, $\bar{\beta}_{i,0}$ and $\bar{\beta}_{o,i}$ in Eqs. (A4) and (B4) are the cylindrical translation matrix accommodating the possibility of shifting the ith row to the right or the left. For further information on how to use and construct these matrices, see [18].

APPENDIX C. GENERALIZED SCATTERING (TRANSMISSION) MATRIX METHOD

We expand any field Ψ as

$$\psi_i(\mathbf{r}) = \bar{\bar{\psi}}^{+}(x, y + d_i, z) \cdot \mathbf{a}_i + \bar{\bar{\psi}}^{-}(x, y + d_i, z) \cdot \bar{\mathbf{R}}_{g\,i,i+1} \cdot \mathbf{a}_i, \tag{C1}$$

where $i = 0, 1, \ldots, N_L - 1$ and N_L is the number of layers. Here, we have

$$\bar{\bar{\psi}}^{\pm}(x, y + d_i, z) = \left[e^{-jk_{xm}x \mp jk_{ym}y}\delta_{mn}\right]. \tag{C2}$$

To excite the structure by a single plane wave, we insert

$$\mathbf{a}_0 = [\ \ldots\ \ 0\ \ \ldots\ \ 0\ \ 1\ \ 0\ \ \ldots\ \ 0\ \ \ldots\ ]^T. \tag{C3}$$

We remind the reader that the propagation constants k_{xm} k_{ym} are defined by equations similar to Eq. (16).

The generalized reflection matrices in Eq. (C1) are calculated recursively in the following manner

$$\bar{\mathbf{R}}_{g\,i,i+1} = \bar{\mathbf{R}}_{i,i+1} + \bar{\mathbf{T}}_{i+1,i} \cdot \bar{\mathbf{D}}_{i+1} \cdot \bar{\mathbf{R}}_{g\,i+1,i+2} \cdot \bar{\mathbf{M}}_{i+1}^{-1} \cdot \bar{\mathbf{D}}_{i+1} \cdot \bar{\mathbf{T}}_{i,i+1}, \tag{C4}$$

where

$$\bar{\mathbf{M}}_{i+1} = \bar{\mathbf{I}} - \bar{\mathbf{D}}_{i+1} \cdot \bar{\mathbf{R}}_{i+1,i} \cdot \bar{\mathbf{D}}_{i+1} \cdot \bar{\mathbf{R}}_{g\,i+1,i+2},\ \bar{\mathbf{D}}_{i+1} = \left[e^{-jk_{ym}(d_{i+1}-d_i)}\delta_{mn}\right], \tag{C5}$$

$$\mathbf{a}_{i+1} = \bar{\mathbf{M}}_{i+1}^{-1} \cdot \bar{\mathbf{D}}_{i+1} \cdot \bar{\mathbf{T}}_{i,i+1} \cdot \mathbf{a}_i, \mathbf{a}_N = \bar{\mathbf{T}}_{N-1,N} \cdot \mathbf{a}_{N-1}, \tag{C6}$$

$$\mathbf{a}_N = \left(\prod_{i=N-1}^{0} \bar{\mathbf{M}}_{i+1} \cdot \bar{\mathbf{D}}_{i+1} \cdot \bar{\mathbf{T}}_{i+1,i}\right) \cdot \mathbf{a}_0, \tag{C7}$$

while the initial condition is given by $\bar{\mathbf{R}}_{g\,N,N+1} = 0$.

REFERENCES

1. Iijima, S., "Helical microtabules of graphitic carbon," *Nature*, Vol. 354, 56–58, 1991.
2. Meyyappan, M., *Carbon Nanoyubes: Sceince and Applications*, CRC Press, 2005.
3. Poole, C. P. and F. J. Owens, *Introduction to Nanotechnology*, Wiley-Interscience, 2003.
4. Smalley, R. E., M. S. Dresselhaus, G. Dresselhaus, and P. Avouris, *Carbon Nanotubes: Synthesis, Structure, Properties and Applications*, Springer, 2001.
5. Kempa, K., et al., "Photonic crystals based on periodic arrays of aligned carbon nanotubes," *Nano Letters*, Vol. 3, No. 1, 13–18, 2003.
6. Lidorikis, E. and A. C. Ferrari, "Photonics with multiwall carbon nanotube arrays," *ACS Nano*, Vol. 3, No. 5, 1238–1248, 2009.
7. Butt, H., Q. Dai, T. D. Wilkinson, and G. A. J. Amaratunga, "Negative index photonic crystal lenses based on carbon nanotube arrays," *Photonics and Nanostructures — Fundamentals and Applications*, Vol. 10, No. 4, 499–505, October 2012.
8. Slepyan, G. Y., et al., "Electronic and electromagnetic properties of nanotubes," *Phys. Rev. B*, Vol. 57, No. 16, 9485–9497, April 1998.
9. Slepyan, G. Y., et al., "Electrodynamics of carbon nanotubes: dynamic conductivity, impedance boundary conditions, and surface wave propagation," *Phys. Rev. B*, Vol. 60, No. 24, 17136–17149, December 1999.
10. Slepyan, G. Ya., M. V. Shuba, and S. A. Maksimenko, "Theory of optical scattering by achiral carbon nanotubes and their potential as optical nanoantennas," *Phys. Rev. B*, Vol. 73, 195416–19526, May 2006.
11. Mikki, S. M. and A. Kishk, "Theory of optical scattering by carbon nanotubes," *Microwave & Optical Technology Letters*, Vol. 49, No. 10, 2360–2364, October 2007.
12. Mikki, S. M. and A. A. Kishk, "Derivation of the dielectric tensor of carbon nanotubes using lattice dynamics formalism," *Progress In Electromagnetics Research B*, Vol. 9, 1–26, 2008.
13. Mikki, S. and A. Kishk, "Electromagnetic scattering by multi-wall carbon nanotube using effective-boundary condition approach," *IEEE Antennas & Propagation/URSI International Symposium*, 2008.

14. Mikki, S. M. and A. A. Kishk, "Electromagnetic scattering by multi-wall carbon nanotubes using effective-boundary condition approach: Theory and applications," *Progress In Electromagnetics Research B*, Vol. 17, 49–67, 2009.
15. Mikki, S. M. and A. A. Kishk, "A symmetry-based formalism for the electrodynamics of nanotubes," *Progress In Electromagnetics Research*, Vol. 86, 111–134, 2008.
16. Mikki, S. M. and A. A. Kishk, "Various homogenization formalisms for carbon nanotube composites," *International URSI Meeting*, Ottawa, July 21–26, 2007.
17. Mikki, S. M. and A. Kishk, "Mean-field electrodynamic theory of aligned carbon nanotube composites," *IEEE Trans. Antennas Progat.*, Vol. 57, No. 5, 1412–1419, May 2009.
18. Chew, W. C., *Waves and Fields in Inhomogeneous Media*, re-print Edition, IEEE Press, 1999.
19. Kushta, K. and K. Yausumoto, "Electromagnetic scattering from periodic arrays of two circular cylinders per unit cell," *Progress In Electromagnetics Research*, Vol. 29, 69–85, 2000.
20. Yausumoto, K. and K. Yoshitomi, "Efficient calculation of lattice sums for free-space periodic Green's functions," *IEEE Trans. Antennas & Propagation*, Vol. 47, 1050–1055, June 1999.
21. Abramowitz, M. and I. A. Stegun, *Handbook of Mathematical Functions*, Dover Publications, 1965.
22. Collins, P. G., "Defects and disorder in carbon nanotubes," *Oxford Handbook of Nanoscience and Technology: Frontiers and Advances*, A. V. Narlikar, & Y. Y. Fu, (Eds.), Oxford Univ. Press, Oxford, 2009.
23. Nho, H. W., Y. Kalegowda, H.-J. Shin, and T. H. Yoon, "Nanoscale characterization of local structures and defects in photonic crystals using synchrotron-based transmission soft X-ray microscopy," *Scientific Reports*, Vol. 6, 24488, 2016.
24. Liew, S. F., S. Knitter, W. Xiong, and H. Cao, "Photonic crystals with topological defects," *Phys. Rev. A*, Vol. 91, 023811, February 6, 2015.